Available online at www.sciencedirect.com
SCIENCE DIRECT®
ELSEVIER
Journal of Sound and Vibration 275 (2004) 193–221
JOURNAL OF SOUND AND VIBRATION
www.elsevier.com/locate/jsvi

Modelling of a hydraulic engine mount with fluid–structure interaction finite element analysis

Wen-Bin Shangguan*, Zhen-Hua Lu

Department of Automotive Engineering and the State Key Laboratory of Automotive Safety and Energy, Tsinghua University, Beijing 100084, People's Republic of China

Received 30 October 2002; accepted 18 June 2003

Abstract

Hydraulic engine mount (HEM) is now widely used as a highly effective vibration isolator in automotive powertrain. A lumped parameter (LP) model is a traditional model for modelling the dynamic characteristics of HEM, in which the system parameters are usually obtained by experiments. In this paper, a fluid–structure interaction (FSI) finite element analysis (FEA) method and a non-linear FEA technology are used to determine the system parameters, and a fully coupled FSI model is developed for modelling the static and lower-frequency performance of an HEM. A FSI FEA technique is used to estimate the parameters of volumetric compliances, equivalent piston area, inertia and resistance of the fluid in the inertia track and the decoupler of an HEM. A non-linear FEA method is applied to determine the dynamic stiffness of rubber spring of the HEM. The system parameters predicated by FEA are compared favorably with experimental data and/or analytical solutions. A numerical simulation for an HEM with an inertia track and a free decoupler is performed based on the FSI model and the LP model along with the estimated system parameters, and again the simulation results are compared with experimental data. The calculated time histories of some variables in the model, such as the pressure in the upper chamber, the displacement of the free decoupler and the volume flow through the inertia track and the decoupler, under different excitations, elucidate the working mechanism of the HEM. The pressure distribution calculated with the FSI model in the chambers of the HEM validates the assumption that the pressure distribution in the upper and lower chamber is uniform in the LP model. The work conducted in the paper demonstrates that the methods for estimating the system parameters in the LP model and the FSI model for modelling HEM are effective, with which the dynamic characteristic analysis and design optimization of an HEM can be performed before its prototype development, and this can ensure its low cost and high quality for development.

*Corresponding author. Room 221, Building 31, Tsinghua University, Beijing 100084, People's Republic of China. Tel.: +86-10-6277-9096; fax: +86-10-6278-5708. Now at the Department of Automotive Engineering, South China University of Technology, Guangzhou 510641, People's Republic of China.

E-mail address: shangguanwb99@mails.tsinghua.edu.cn, shangguanwb99@tsinghua.org.cn (W.-B. Shangguan).

0022-460X/$ - see front matter © 2003 Elsevier Ltd. All rights reserved.
doi:10.1016/S0022-460X(03)00799-5

1. Introduction

The automobile engine–chassis–body system may undergo undesirable vibrations due to disturbances from the road and the engine. The vibrations induced by the road or the engine at idle are typically at the frequencies below 30 Hz. In order to control the idle shake and the road-induced vibrations, the engine mount should be stiff and highly damped. On the other hand, for a small amplitude excitation over the higher frequency range (30–250 Hz) from the engine, a compliant and lightly damped mount is required for vibration isolation and acoustic comfort. So, the engine mount must satisfy these two essential but conflicting criteria. This disparity between isolation characteristics and control characteristics has profoundly changed the way in which the automobile industry approaches mount design.

A conventional rubber mount cannot satisfy the conflicting requirements simultaneously as the lumped stiffness and the viscous damping are nearly invariant with excitation amplitudes and frequencies over the concerned excitation range (1–250 Hz). Consequently, at present, manufactures have increasingly used hydraulic engine mount (HEM), whose stiffness and damping characteristics can vary with excitation frequencies and amplitudes.

A typical HEM is illustrated in Fig. 1. At the top (A), the mount contacts the automobile engine, and at the bottom (B) it connects with car chassis. The HEM contains two rubber components (the rubber spring and rubber bellow), an upper and a lower fluid chamber, an inertia track and a free decoupler. The fluid in the mount is usually water mixed with ethylene glycol. For low-frequency and large-amplitude excitations from the road or from the engine at idle, the rubber spring pumping action causes the free decoupler to reach the top or bottom constraint of the decoupler cage, and the fluid is forced to flow back and forth between two chambers mainly through the inertia track. Thus the HEM provide a large stiffness and damping at this time. For high-frequency and small-amplitude excitation from the engine, fluid travels only around the

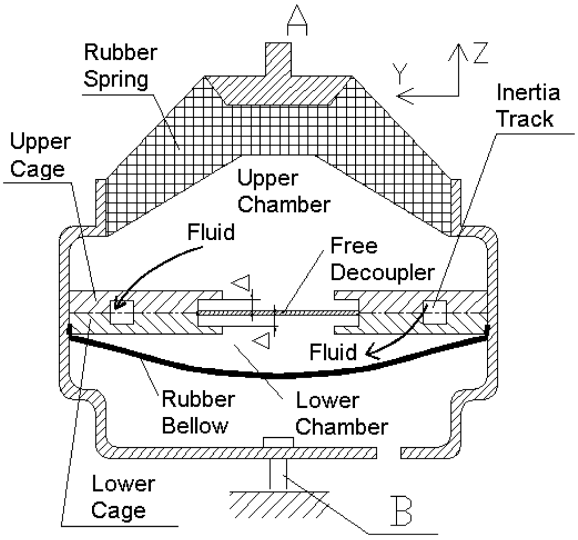

Fig. 1. Cross-section of a HEM with a free decoupler and an inertia track.

decoupler, and causes the mount to behave as an elastomeric mount. So, in this simple passive isolation device, the stiffness and the damping are different for various excitation frequencies and amplitudes.

A detailed discussion on engine vibration and desirable engine mount characteristics are presented by Yu et al. [1,2]. The authors in Refs. [3–9] also present a complete literature survey on the property descriptions and the modelling methods for HEMs with lumped parameter model. Hence there is no need to re-convey what has been stated already. The focus now turns into the method for obtaining the system parameters in the lumped parameter model. The method for measuring fluid chamber compliances and inertia and resistance of the fluid in the inertia track are presented by Kim and Singh [4]. Some analytical solutions for the compliance of the upper fluid chamber with the rubber spring of regular configuration, and for the fluid resistance of the inertia track are also given by Singh and Kim [5]. Muller [10] mentions that dynamic stiffness, upper fluid chamber compliance and equivalent piston area can be calculated by FEA, but only a simple model and some results are given. Foumani et al. [22] use finite element technique and ANSYS 5.7 to calculate the upper chamber compliance. The parameters of volumetric compliances, bulge damping and equivalent piston area of the rubber spring are obtained experimentally by Geisberger et al. [3], and the system parameters for the inertia track and decoupler are also predicted by a unique experimental set-up and parameter identification technique. Moreover, they provide a deep insight into the physics of a hydraulic mount. For most of these methods, a prototype of one HEM and interrelated parts must be fabricated to estimate the system parameters.

Instead, this paper applies fluid–structure interaction (FSI) finite element analysis (FEA) and non-linear FEA to determine the system parameters. An FSI FEA technique is used to estimate the upper fluid chamber compliance, the equivalent piston area, the inertia and the resistance of the fluid in the inertia track and the free decoupler of an HEM. A non-linear FEA method is applied to determine the dynamic stiffness of the rubber spring of the HEM. The estimated parameters fit well with the experimental data and/or analytical solutions. Moreover, a fully coupled FSI model is developed for modelling the static performance and lower-frequency response of one HEM with an inertia track and a decoupler. With the methods proposed in this paper, only stress–strain of the rubber material and the fluid constants, such as the density and viscosity, and the sizes of the HEM are needed for estimating the system parameters in the LP model and predicting the response of the HEM. To the best of the author's knowledge, this is the first time that FSI FEA techniques are used in the modelling of the HEM in detail. The static performance of the HEM is analyzed with the FSI model. A numerical simulation for the HEM is performed for the two cases of low-frequency and large-amplitude excitations with the LP model and the FSI model, and high-frequency and small-amplitude excitations with the LP model. A comparison between the calculation and the experiment proves that the methods proposed in this paper are effective for the concerned excitation amplitude and frequency range of 1–200 Hz. The time histories of some variables in the model, such as the pressure in the upper chamber, the displacement of the decoupler and the volume flow across inertia track and around the decoupler, are also presented, which give us a better understanding of the working mechanism of HEM. Enhancement of this paper to already published papers is that with the proposed methods for modelling HEM, no prototype mounts and parts need to be manufactured in the design stages, thus it will help engineers in reducing mount design time.

2. Fundamental theory for FSI FEA

In FSI analysis, fluid forces are applied to the solid, and the solid deformation changes the fluid domain. Difficulties of the FSI analysis arise not only because the governing equations for fluid are non-linear, but also because the governing equations for fluid and structure are described in different co-ordinates. With new algorithms for fluid FEA, such as SU/PG [11], GLS [12] and Talor-Galerkin [13] et al., and the application of arbitrary Lagrangian–Eulerian (ALE) to the Navier–Stokes (N–S) equations for fluid motion by Nomura, Hughes [14] and Bathe [15] et al. since 1990, the large displacement boundary motion for fluid can be included in the calculation, and this makes non-linear FSI FEA possible. At present, some commercial software, such as ADINA [16], has strong capability for FSI analysis. The technique of FSI FEA and general purpose programs have been used widely in the area of nuclear, offshore, biomechanics, aerospace and aeronautics etc. [17].

2.1. Mathematical model

The solid response is modelled using the standard Lagrangian formulation for large displacement and large strain. The governing field equations are

$$\tau_{ij,j} + f_i^B = \rho_s \ddot{u}_i, \tag{1}$$

where τ_{ij} is the ijth components of the Cauchy stress tensor for $(i,j = 1,2,3)$, $\ddot{u}_i$ the material particle acceleration in the co-ordinate i direction, ρ_s the mass density of the solid, f_i^B the component of the body force, and a comma is used to signify partial differentiation. The Ogden material model for incompressible materials is used to describe the constitutive behavior of rubber components in the HEM, such as the rubber spring and the rubber bellow. The model assumes a strain energy density per unit original volume of the following form [18]

$$U = \sum_{n=1}^{3} \frac{\mu_n}{\alpha_n} (\lambda_1^{-\alpha_n} + \lambda_2^{-\alpha_n} + \lambda_3^{-\alpha_n} - 3), \tag{2}$$

where

$$\lambda_1 \lambda_2 \lambda_3 = 1 \tag{3}$$

α_n and μ_n are material constants determined from experiment, and λ_i $(i = 1,2,3)$ is the principal value of the stretch tensor. The procedures in determining α_n and μ_n are [18,19]: (1) Measure the tensile and compress engineering stress–strain form dumbbell and cylinder specimen of the rubber materials, respectively; if possible, carry out equibiaxial extension and shear tests. (2) Calculate the engineering stress corresponding to the strain energy density U [19]. (3) Obtain α_n and μ_n by fitting the engineering stress–strain obtained from experiment and calculation using least-squares method.

The fluid response is modelled using the full N–S equations assuming incompressible flow. In ALE form, the N–S equations are given in Refs. [14,16], that is

Continuity

$$u_{i,i} = 0 \tag{4}$$

Momentum

$$\rho \frac{\partial u_i}{\partial t} + \rho(u_j - u_{mj}) \frac{\partial u_i}{\partial x_j} = \frac{\partial \tau_{ij}}{\partial x_j} + f_i, \tag{5}$$

where ρ is the constant mass density of the fluid, u_i is a component of velocity, u_{mj} is the velocity of moving mesh and we may arbitrarily specify u_{mj} in the fluid domain, f_i is a component of the body force vector, and τ_{ij} is the ijth component of the stress tensor defined as

$$\tau_{ij} = -p\delta_{ij} + \mu(u_{i,j} + u_{j,i}), \tag{6}$$

where p is the fluid pressure, δ_{ij} the Kronecker delta, and μ the coefficient of viscosity.

2.2. Finite element solutions [16]

The boundary conditions applied to the fluid–structure interfaces are

$$\underline{\mathbf{d}_f} = \underline{\mathbf{d}_s}, \quad \mathbf{n} \bullet \underline{\boldsymbol{\tau}_f} = \mathbf{n} \bullet \underline{\boldsymbol{\tau}_s}, \tag{7}$$

where $\mathbf{d}_f$ and $\mathbf{d}_s$ are, respectively, the fluid and solid displacements, and $\boldsymbol{\tau}_f$ and $\boldsymbol{\tau}_s$ are, respectively, the fluid and solid stresses. The underlining denotes that the values are defined on the fluid–structure interfaces only.

After the finite element spatial discretization of the ALE N–S Eqs. (4)–(6) and solid Eqs. (1)–(3), and application of the boundary conditions (7) to the discrete finite element equations of the fluid and the structure, the coupled fluid-structure system equations are obtained and expressed as

$$\mathbf{F}(\mathbf{X}) = \begin{bmatrix} \mathbf{F_f}[\mathbf{X_f}, \underline{\mathbf{d}_s}(\mathbf{X_s})] \\ \mathbf{F_s}[\mathbf{X_s}, \underline{\boldsymbol{\tau}_f}(\mathbf{X_f})] \end{bmatrix} = \mathbf{0}, \tag{8}$$

where $\mathbf{X} = (\mathbf{X_f}, \mathbf{X_s})^{\mathbf{T}}$ are the solution vectors of the coupled system, $\mathbf{X_f}$ and $\mathbf{X_s}$ the fluid and solid vectors defined at the fluid and solid nodes, respectively, $\mathbf{F_f}$ and $\mathbf{F_s}$ the finite element equations corresponding to the fluid and the structure model. In the ADINA program, we can choose direct or iterative solution to Eq. (8). In this study, the direct method is adopted, since it is faster than iterative method.

In FSI analysis with ADINA, the fluid model and the structure model are defined solely; the interfaces between fluid and structure are defined as coupled faces. The two models can be meshed with different elements and different sizes, the nodal point positions of the two models are therefore generally not the same on the fluid–structure interfaces. In the coupled faces, the fluid nodal displacements are interpolated using the solid nodal displacements, and the fluid traction at a solid node is interpolated using the stress of the fluid boundary element where the solid node is located. The coupling requires force equilibrium and velocity and displacement compatibility at the fluid–structure interface at each time step in the analysis. To satisfy these conditions, iteration is performed between the fluid and the solid solvers at each time step until sufficient convergence has been reached [16].

3. Lumped parameter model

Fig. 2 is the lumped parameter model for the HEM illustrated in Fig. 1 [3]. In Fig. 2, K_r and B_r are the dynamic stiffness and damping properties of the rubber spring, respectively. The rubber spring also functions as a piston with an effective piston area A_p. Finally, the rubber spring adds volumetric compliance to the model, represented by C_1. The fluid in the inertia track is assigned lumped parameters I_i, R_{i1} and R_{i2} representing the inertia, and linear and non-linear resistance, respectively. Similarly, we assign lumped parameters I_d, R_{d1} and R_{d2} to the decoupler. The lower chamber contributes to the volumetric compliance and is modelled using a lumped parameter C_2. Variables in the model include the input excitation $x(t)$, the transmitted force to the mount base $F(t)$, and the flow through the inertia track $Q_i(t)$ and the decoupler $Q_d(t)$. Also, the pressures in the upper and the lower chambers are captured by $P_1(t)$ and $P_2(t)$, respectively.

The dynamic equations for the lumped model in Fig. 2 can be derived easily according to continuity and momentum equations. The continuity equations are [3,4]

$$C_1\dot{P}_1 = A_p\dot{x} - Q_i - Q_d, \quad C_2\dot{P}_2 = Q_i + Q_d. \tag{9}$$

The momentum equation of the fluid in the inertia track is [3,4]

$$P_1 - P_2 = I_i\dot{Q}_i + (R_{i1} + R_{i2}|Q_i|)Q_i. \tag{10}$$

The linear and non-linear resistance, R_{i1} and R_{i2}, depend on the configuration and roughness of the inertia track, and the viscosity of the fluid. They are difficult to estimate by analytical solutions. The inertia I_i is defined as

$$I_i = M_i/A_i^2, \tag{11}$$

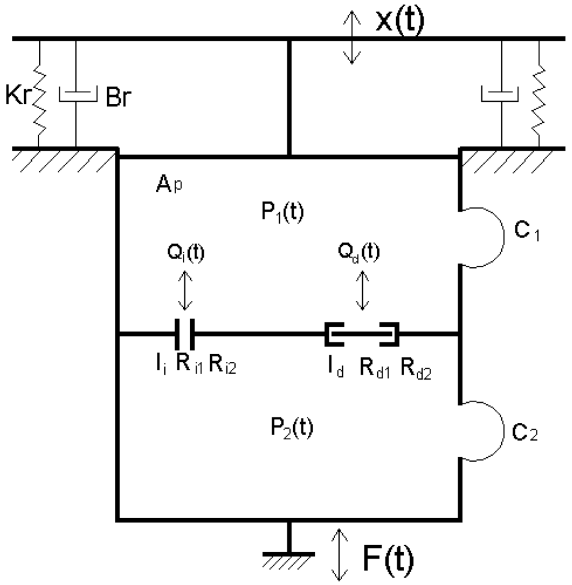

Fig. 2. A lumped parameter model of HEM.

where M_i and A_i are the fluid mass in the inertia track and the cross-section area of the inertia track, respectively.

The moment equation of the free decoupler is [3,6]

$$P_1 - P_2 = I_d\dot{Q}_d + (R_{d1} + R_{d2}|Q_d| + R_{inf})Q_d. \tag{12}$$

As with the inertia track, the decoupler inertia I_d is assumed constant, and the free decoupler resistance includes the linear and non-linear parameters, denoted by R_{d1} and R_{d2}, respectively. The constant R_{inf} in Eq. (12) depends on the position of the decoupler. When flow is oscillating across the decoupler orifice, the decoupler is considered uncoupled and in this case, R_{inf} should be zero. As the free decoupler reaches the top or bottom constraints of the cage, all flow across the decoupler is blocked and the decoupler is considered coupled. In order to model this flow-stopping effect, R_{inf} should be infinite for this moment. In this paper, we use a polynomial expression to describe the behavior of the decoupler.

$$R_{inf} = E\left(\frac{x_d}{\Delta}\right)^{\gamma}, \tag{13}$$

where E is a positive constant, γ is a positive odd constant, x_d is the displacement of the decoupler, Δ is the half-distance of the decoupler free travel gap.

Under the displacement excitation, $x(t)$, the transmitted force, $F(t)$, is obtained from Ref. [3]

$$F(t) = \begin{cases} K_r x + B_r\dot{x} + A_p(P_1 - P_2) + A_p P_2 & \text{if the decoupler contacts the cage} \\ K_r x + B_r\dot{x} + (A_p - A_d)P_1 + A_p P_2 + A_d(R_{d1} + R_{d2}|Q_d|)Q_d & \text{if the decoupler is free} \end{cases} \tag{14}$$

The complex stiffness of the HEM at an excitation frequency ω_0 is expressed as [5]

$$K(\omega) = \mathcal{F}(F(t))/\mathcal{F}(x(t))|_{\omega=\omega_0} = K_s + \mathrm{j}K_l = K_s + \mathrm{j}\omega D, \tag{15}$$

where $\mathcal{F}$ represents the Fourier transformations. K_s is the storage stiffness, K_l is the loss stiffness and D is the damping coefficient. Dynamic stiffness K_d and loss angle ϕ are defined as

$$K_d = \sqrt{K_s^2 + K_l^2}, \quad \phi = \mathrm{arctg}(K_l/K_s). \tag{16}$$

The dynamic properties of HEM are usually characterized by K_d, and ϕ or D.

The dynamic stiffness and the damping of the rubber spring are almost invariant with the excitation amplitudes and frequencies, and the dynamic stiffness is about 1.2–1.6 times of its static stiffness [20]. The loss angle of the rubber spring is small and is usually about 3–6°. So the dynamic stiffness K_r and damping B_r can be roughly regarded as constants. The lower chamber compliance C_2 depends on the thickness of the rubber bellow, which is very thin and about 2 mm in general. Hence the C_2 is much larger than the C_1, and we often set $C_2 = C_1 \times 10^3$. When the configuration of the inertia track is regular, the inertia I_i can be obtained from the Eq. (11). The system parameters K_r, C_1, A_p, R_{i1}, R_{i2}, I_d, R_{d1} and R_{d2} are generally measured by experiments or estimated with some approximation analytical solutions in Refs. [3–9]. But in this paper we use non-linear FEA and FSI FEA technique to obtain the parameters.

4. Determination of the system parameters in the lumped model

4.1. The dynamic stiffness of the rubber spring

Firstly, the static stiffness of the rubber spring is obtained with the non-linear FEA, and then the dynamic stiffness is estimated from Ref. [20]

$$K_d = fK_s, \tag{17}$$

where K_d and K_s are the dynamic and static stiffness, respectively, and f is a correction factor that is generally in the range from 1.2 to 1.6.

Fig. 3 is the cross-section of the rubber spring in an HEM. There is one metal inserter in the rubber spring, which servers as load bearing. The deformation of the metal inserter can be ignored compared with that of the rubber, so the inserter is generally excluded in the FEM model of the rubber spring [21], and only the corresponding displacement constraint equations related to faces A, B, C and D are imposed. The constraint conditions, that the nodal displacements in Z direction on faces A, B, C and D are equivalent and the displacements in X and Y directions in these faces are zero, must be assumed in the FEM model when the relationship of the vertical deflection and the vertical force on the face A of the rubber spring is to be found. The outer face of the rubber spring, the face E, is connected to one metal component fixed in the chassis, so all the nodal displacements in the face are set to zero.

A complete three-dimensional structure of the rubber spring is modelled with the ADINA-M module, and the FEM mesh is shown in Fig. 4. A Delauray mesher is used for generation of elements on the geometry. The rubber spring is discretized by the 8/1 element (8-nodes hexahedral

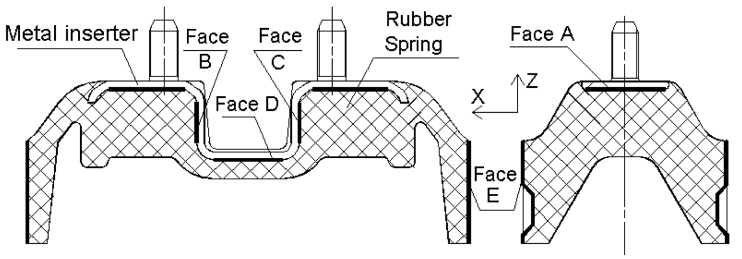

Fig. 3. Cross-section of the rubber spring.

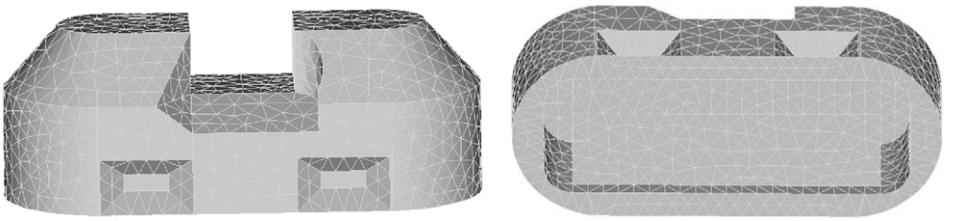

Fig. 4. FEM model for the rubber spring.

element with one pressure variable), and the maximum size for the element is 4 mm. The total nodes and elements in the FEM model are 9763 and 16171, respectively.

Ogden hyperelastic model with $N = 3$ is used to characterize the highly non-linear and incompressible rubber material. The experimental stress–strain curve shown in Fig. 5 is fit using a standard least-squares approximation available in ADINA, which automatically determines the appropriate Ogden model constants in Eq. (2). Fig. 5 shows that the fitting is accurate up to a strain of 120%, which is adequate for analysis.

The force–displacement curves in Z direction obtained from FEM and experiment are shown in Fig. 6. The calculated and tested static stiffness of the rubber spring are 290.3 and 279.2 N/mm, respectively, which agree well with each other.

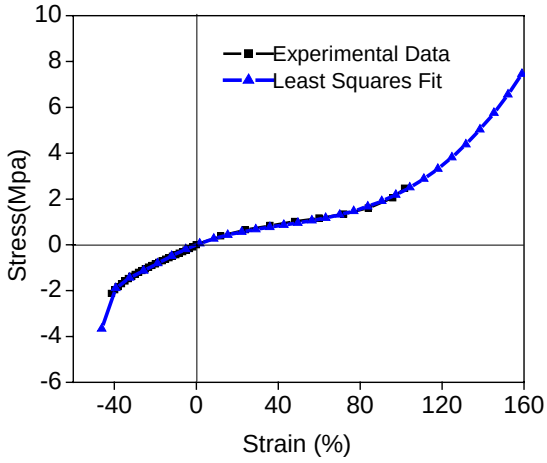

Fig. 5. Experimental stress–strain curve and the least-squares fit curve.

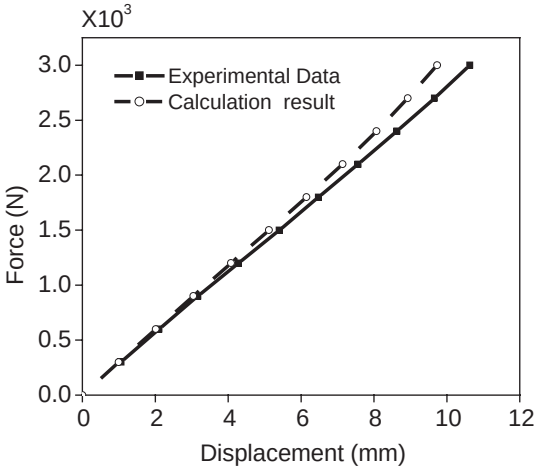

Fig. 6. Vertical force–displacement curve for the rubber spring.

In estimating the other system parameters as follows, the material constitutive model for the rubber spring and rubber bellow is 3-term Ogden model.

4.2. The upper fluid chamber compliance

The FSI finite element meshes for predicting the compliance are shown in Fig. 7, where 7376 8-node elements (the 8/1 element) for the structure and 18,094 4-node elements for the fluid are used to mesh the coupled system. The maximum size of the element for structure and fluid model is 6 millimeters, and the total number of nodes is 7847, which includes 4028 nodes for the structure model and 3819 for the fluid model. The density and viscosity of the fluid are regarded as constants. The interior faces of the rubber spring and the corresponding contacting faces in the fluid model are defined as the FSI interfaces. A uniform velocity load, V_L, is applied on the lower face of the fluid model in 1 or 2 s as shown in Fig. 7(b). The other faces in the fluid model are regarded as rigid walls without slip. The boundary conditions of the rubber spring are that the nodal displacements on face A, B, C, D and E of the rubber spring are assumed to be zero in the model.

The compliance C_1 is defined as

$$C_1 = \Delta V_1/\Delta P_1, \tag{18}$$

where ΔV_1 is the volume change of the upper chamber due to the pressure change, ΔP_1. The volume of the chamber, V_1, is obtained from

$$V_1 = V_L A t, \tag{19}$$

where A is the area of the bottom face of the fluid model, and t is the time for applying the velocity load.

Under the velocity load, a pressure P_1 is built up in the upper chamber since the fluid is incompressible, and thus causes the rubber spring to bulge. The chamber pressure can be obtained from the FSI FEA. Because the velocity load is applied in a relatively long period, the pressures of all nodes in the fluid model are identical. For different velocity loads, the relationships between the pressure and the volume of the upper chamber can be got by means of the method stated above.

Fig. 8 shows the relationships between the pressure and volume in the upper chamber from calculation and experiment. The experimental procedures for measuring the pressure versus

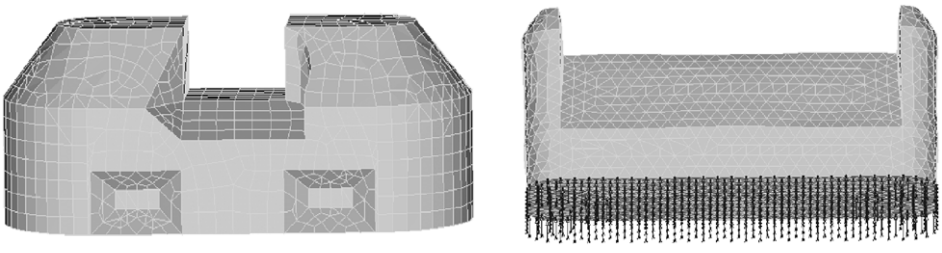

(a) (b)

Fig. 7. The FSI FEA models for upper chamber compliance. (a) The structural model. (b) The fluid model.

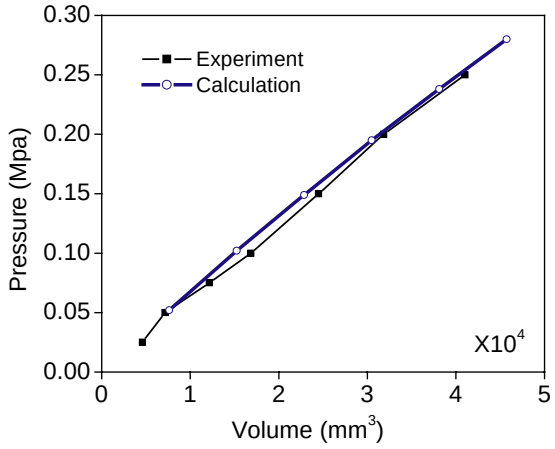

Fig. 8. The volume versus pressure for the chamber.

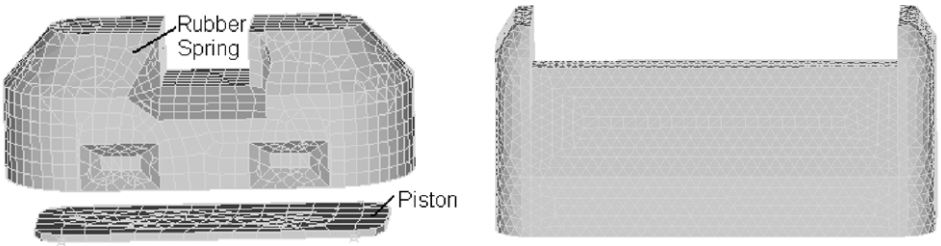

Fig. 9. FSI FEA meshes for equivalent piston area. (a) The structural model. (b) The fluid model.

volume relationships proposed by Kim etc. [4] are utilized in this study. The compliances from experiment and FSI FEA are 1.65×10^5 and $1.6 \times 10^5\,\mathrm{mm}^5/\mathrm{N}$, respectively, which indicates a good agreement between the results.

4.3. The equivalent piston area

The FSI FEA meshes for estimating the equivalent piston area of the rubber spring are shown in Fig. 9. The piston in the structural model is made of steel, and can move only in Z direction. It has one rigid body mode, corresponding to the translation in Z direction. We remove this mode by attaching the piston to ground using a soft spring with the stiffness of $1.0 \times 10^{-11}\,\mathrm{N/m}$. The contacting faces between the interior faces of the rubber spring and the faces in the fluid, and the upper face of the piston and the bottom face of the fluid, are defined as FSI interfaces. The other faces in the fluid models are rigid walls without slip. The boundary conditions of the rubber spring in Fig. 9(a) are the same as those in Fig. 4.

A steady-state displacement load in Z direction, x_r, is applied to the face A of the rubber spring, and the piston displacement, x_p, is obtained with the FSI FEA.

The volume of the fluid chamber, V_r, is obtained from

$$V_r = x_p A_p, \tag{20}$$

where A_p is the area of the piston upper face. The equivalent piston area is predicted by V_r/x_r. Since the piston is attached to the ground with a very soft spring, the pressure in the fluid is almost zero under the displacement load, so that the rubber spring may not undergo bulge deformation.

The equivalent piston area versus the vertical displacement relationship of the rubber spring is given in Fig. 10. It is shown that the area can be regarded as a constant when the vertical displacement is larger than 2 mm.

The upper chamber compliance can also be calculated from the FSI FEA model shown in Fig. 9. We assign the boundary conditions of the rubber spring model in Fig. 7(a) to the rubber spring model in Fig. 9(a). Then a steady state displacement load, S, in Z direction is applied to the piston, and the volume of the chamber V_1 is calculated from

$$V_1 = A \times S, \tag{21}$$

where A is the area of the piston upper face. The pressure in the chamber is then estimated by FSI FEA. For a sequence of displacement load, the chamber pressure versus volume relationships are obtained. Eq. (18) is then used to calculate the chamber compliance. The compliance predicted from the FSI FEA model in Fig. 9 is $1.61 \times 10^5\,\mathrm{mm}^5/\mathrm{N}$, and the experimental data is $1.65 \times 10^5\,\mathrm{mm}^5/\mathrm{N}$, which validates the FSI FEA model for estimating equivalent piston area. Consequently, the calculated equivalent piston area of rubber spring is acceptable. Because a piston is added to the structural model, the computing time of the model in Fig. 9 is longer than that of the model in Fig. 7 for the compliance estimation.

4.4. The inertia and the resistance of the fluid in the inertia track

The inertia and the resistance can be obtained with the following procedures [3] if the pressure differential of the two ends in the inertia track, $\Delta P = P_1 - P_2$, and the corresponding flow, Q_i are determined by calculation or experiment.

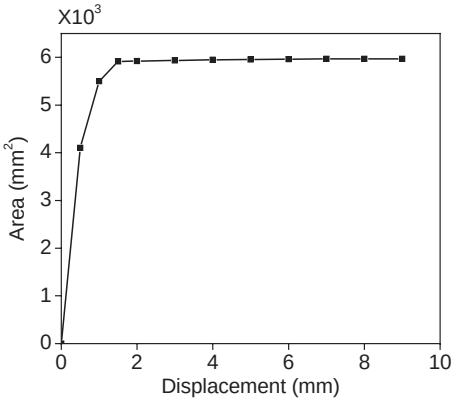

Fig. 10. The equivalent piston area versus the vertical displacement of the rubber spring.

The pressure differential, the flow and the derivative of the flow at time τ are assigned to ΔP^{τ}, Q_i^{τ} and $\dot{Q}_i^{\tau}$, respectively. For a sequence of time denoted by 1,2,3,…, and n, the following moment equations of the fluid in the inertia track are met.

$$\begin{bmatrix} \Delta P^1 \\ \Delta P^2 \\ \cdots \\ \Delta P^n \end{bmatrix} = \begin{bmatrix} \dot{Q}_i^1 & Q_i^1 & |Q_i^1|Q_i^1 \\ \dot{Q}_i^2 & Q_i^2 & |Q_i^2|Q_i^2 \\ \cdots & \cdots & \cdots \\ \dot{Q}_i^n & Q_i^n & |Q_i^n|Q_i^n \end{bmatrix} \begin{bmatrix} I_i \\ R_{i1} \\ R_{i2} \end{bmatrix}. \tag{22}$$

By assigning each matrix to the notation

$$Y = \begin{bmatrix} \Delta P^1 \\ \Delta P^2 \\ \cdots \\ \Delta P^n \end{bmatrix}, \quad U = \begin{bmatrix} \dot{Q}_i^1 & Q_i^1 & |Q_i^1|Q_i^1 \\ \dot{Q}_i^2 & Q_i^2 & |Q_i^2|Q_i^2 \\ \cdots & \cdots & \cdots \\ \dot{Q}_i^n & Q_i^n & |Q_i^n|Q_i^n \end{bmatrix}, \quad \beta = \begin{bmatrix} I_i \\ R_{i1} \\ R_{i2} \end{bmatrix} \tag{23}$$

the least-squares parameter estimation is then applied using

$$\beta^* = (U^{\mathrm{T}}U)^{-1}U^{\mathrm{T}}Y, \tag{24}$$

where β^* is the least-squares estimate of the parameters in β.

Geisberger, Khajepour and Golnaraghi [3] apply a unique experimental set-up to measure the relationship between ΔP^{τ} and Q_i^{τ}, and the parameter identification technique narrated above is used to estimate the inertia and the resistance. In this study, we use FSI FEA technique to determine the flow versus pressure relationships. The geometry models and the meshes of the FSI FEA for the structure and the fluid are shown in Figs. 11 and 12, respectively. For the structural model, the rubber bellow, the interior faces contacting the fluid are defined as FSI interfaces. The upper face of the rubber bellow is fixed. The fluid model consists of the upper and the lower fluid chambers, and the inertia track. A hole, the small face, in the bottom face of the upper chamber connects with the entrance of the inertia track. The pressure load is applied to the top face of the upper chamber. The other faces in the upper chamber are rigid walls without slip. The entrance and the exit of the inertia track are linked with the exit of the upper chamber and the entrance of the lower chamber with the command 'Face Link' of the ADINA. The remaining faces in the inertia track are rigid walls without slip. The bigger face of the top face in the lower chamber is

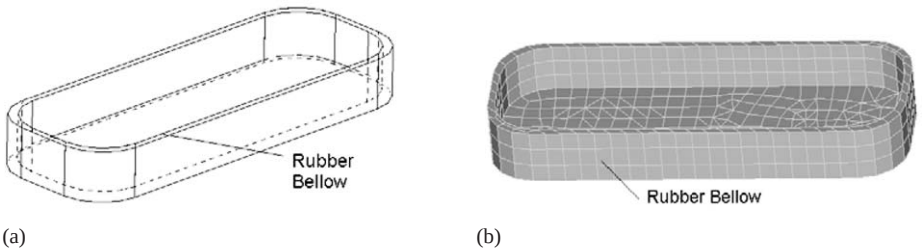

Fig. 11. The structural model to calculate the inertia and the resistance of the fluid in inertia track. (a) Geometry model. (b) FEM model.

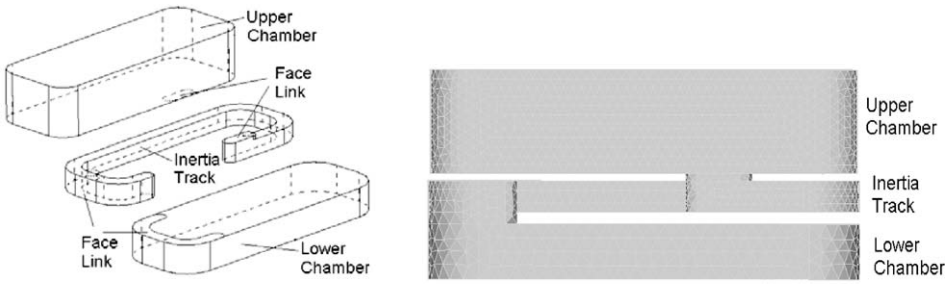

Fig. 12. The fluid model to calculate the inertia and the resistance of fluid in inertia track. (a) Geometry model. (b) FEM model.

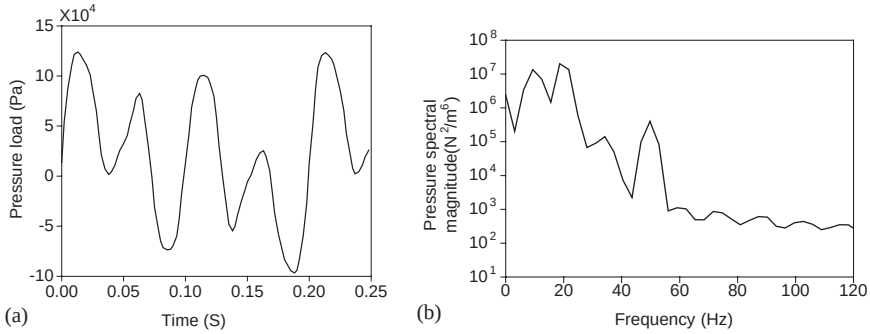

Fig. 13. Pressure excitation. (a) Time history of the random pressure excitation. (b) Power spectral density of the pressure excitation.

rigid wall without slip, and the remaining faces contacting the rubber bellow are defined as FSI interfaces.

In the FSI FEA, a pre-pressure, corresponding to the pressure in the HEM when it is subjected to engine static load, is applied firstly, and then a random pressure is applied. The random pressure and its spectrum are shown in Figs. 13(a) and (b), respectively. As Fig. 13(b) indicates that the frequency spectral magnitude of the pressure excitation is within the concerned frequency range (1–50 Hz).

The calculated average pressure in the exit of the inertia track, P_2, and the flow across the inertia track are shown in Figs. 14 and 15, respectively. The average pressure in the entrance of the inertia track, P_1, is the same as the pressure load. Parameter estimation using the Eqs. (22)–(24) identifies $I_i = 1.9084 \times 10^6\,\mathrm{kg/m^4}$, $R_{i1} = 10.2 \times 10^7\,\mathrm{N\,s/m^5}$ and $R_{i2} = 0.3140\,\mathrm{N\,s^2/m^8}$. The inertia I_i obtained from Eq. (11) is $2.08 \times 10^6\,\mathrm{kg/m^4}$, which is very close to the data from parameter estimation.

The pressure load and the estimated pressure with the predicted system parameters and the Eq. (10) are shown in Fig. 16. As seen from the figure, there is a good agreement between the results.

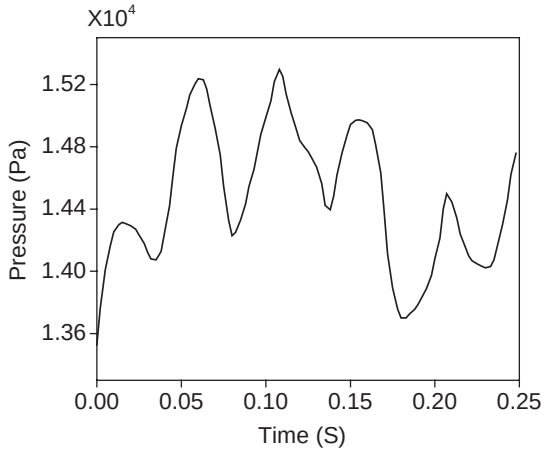

Fig. 14. Pressure in the exit of inertia track.

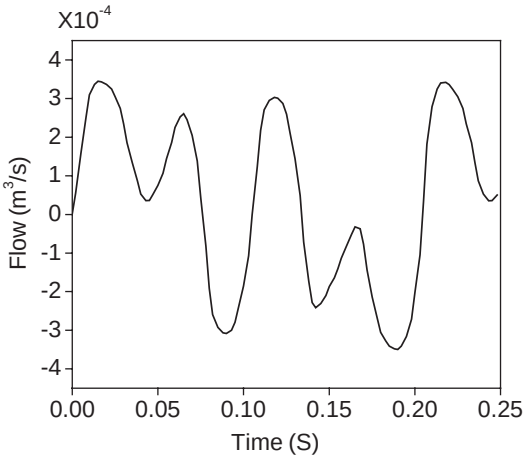

Fig. 15. Fluid flow in the inertia track.

4.5. The inertia and the resistance of the decoupler

If the decoupler moves freely, the moment equation will follow the form

$$P_1 - P_2 = I_d \dot{Q}_d + (R_{d1} + R_{d2}|Q_d|)Q_d \tag{25}$$

which is a reduced form of Eq. (12). The same technique for estimating the parameters of the inertia track is utilized here for estimating the parameters of the decoupler.

The geometry models and the FSI FEA models of the structure and the fluid for calculating the inertia and resistance of the free decoupler are shown in Figs. 17 and 18, respectively. The structural model consists of a free decoupler and a rubber bellow, and the free decoupler is regarded as a rigid body and can move only in Z direction. Only damping force acts on the

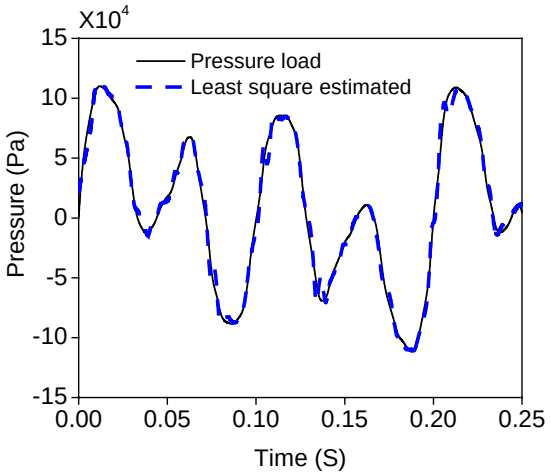

Fig. 16. The estimated pressure load.

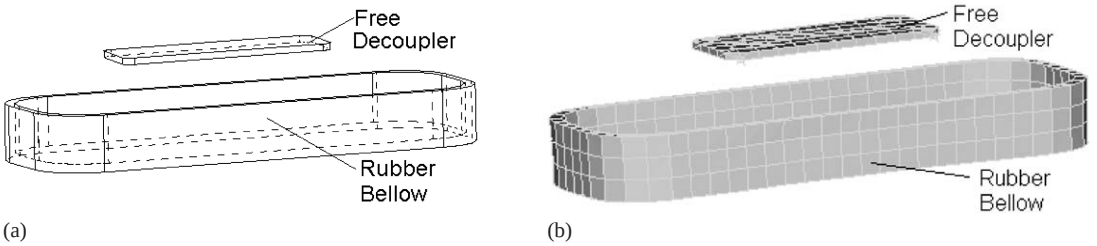

Fig. 17. The structural model to calculate the inertia and the resistance of the free decoupler. (a) Geometry model. (b) FEM model.

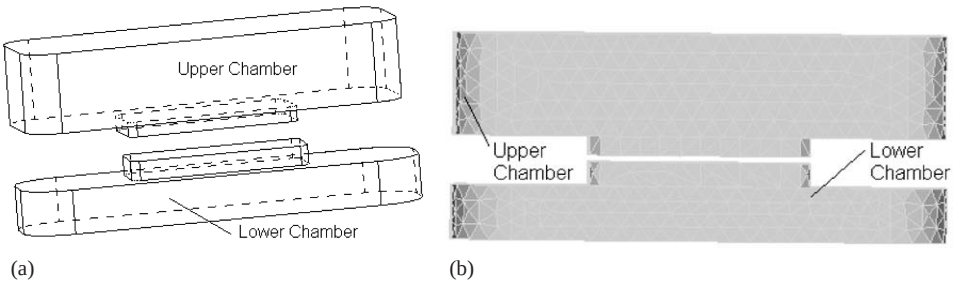

Fig. 18. The fluid model to calculate the inertia and the resistance of the free decoupler. (a) Geometry model. (b) FEM model.

decoupler when it moves within the gap, and if it contacts the cage, a very large force is applied against the decoupler and forces it to stop. In order to describe the behavior of the decoupler, a non-linear spring is used to attach the decoupler to the ground, and the stiffness of the spring has the same expression as Eq. (13).

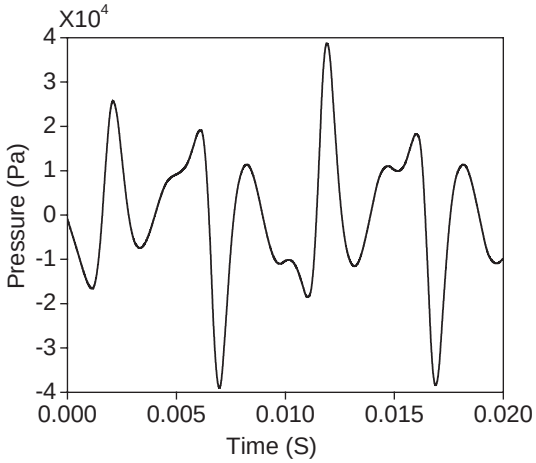

Fig. 19. The pressure excitation.

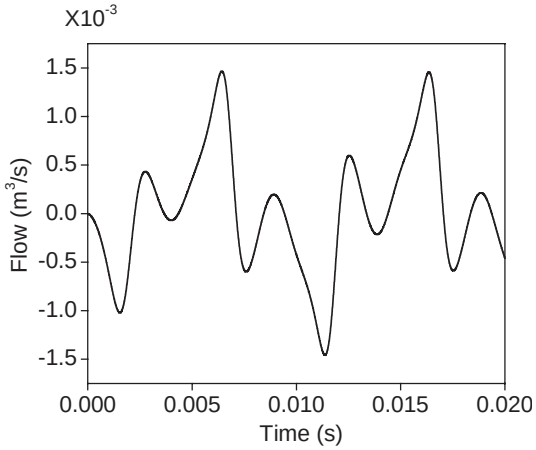

Fig. 20. The fluid flow with decoupler.

The fluid model in Fig. 18 consists of the upper and the lower chambers, and the pressure load is applied to the top face of the upper chamber. The bottom face of the upper chamber contacts the upper face of the decoupler, and it is defined as fluid–structure interface. The other faces in the upper chamber are rigid walls without slip. For the lower chamber, the upper face contacting the lower face of the decoupler, and the faces contacting the rubber bellow are defined as fluid–structure interfaces. The remaining faces are rigid walls without slip.

The time history of the pressure loading is shown in Fig. 19. In comparison with the pressure load in Fig. 13(a), the pressure is much smaller in order to guarantee the decoupler moves within the free gap. Under the pressure load, the flow through the decoupler is estimated with the FSI FEA and is shown in Fig. 20.

The identified parameters using the Eqs. (22)–(24) are $I_d = 1.32 \times 10^4\,\mathrm{kg/m^4}$, $R_{d1} = 3.8 \times 10^6\,\mathrm{N\,s/m^5}$ and $R_{d2} = 47.4\,\mathrm{N\,s^2/m^8}$. The inertia I_d obtained from the division of the decoupler mass and its area is $0.5771 \times 10^4\,\mathrm{kg/m^4}$, and this value is much smaller than the data from identification, which proves that the fluid column moving with the free decoupler has great influence on the HEM's characteristics in high-frequency [3,7].

5. Fully coupled FSI model

The geometry model and the mesh of the structure for the fully coupled FSI model of the HEM with a free decoupler and an inertia track are shown in Fig. 21. The boundary conditions of the rubber spring are the same as those in Fig. 4. The material constitutive model for the rubber spring and rubber bellow is 3-term Ogden model. The behavior of the free decoupler is modelled as the same as that described in Section 4.5. The upper and the low face of the free decoupler

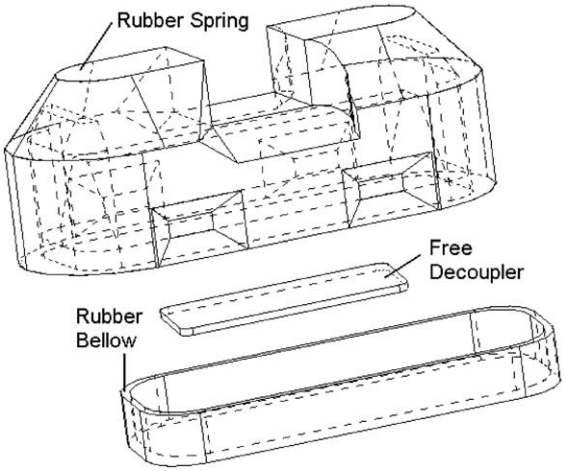

(a)

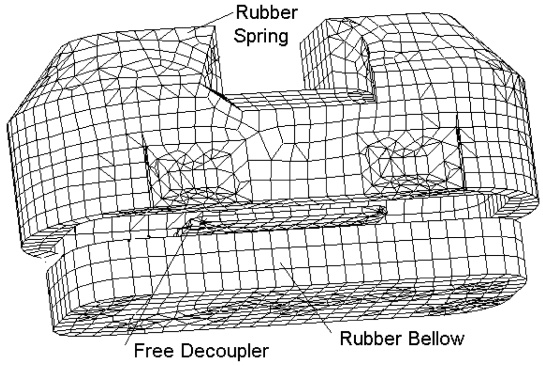

(b)

Fig. 21. The structure model. (a) Geometry model. (b) FEM model.

contacting with the fluid are defined as FSI interfaces, and the other faces are rigid walls without slip. The interior faces of the rubber bellow contacting the fluid are defined as FSI interfaces and the upper face is fixed.

The fluid model is shown in Fig. 22. It consists of the upper and the low chambers and the inertia track. A hole, the small face F1, in the low end of the upper chamber connects with the entrance of the inertia track (face F4), and the face F2 in the low end of the upper chamber contacting with the cage is defined as rigid wall without slip. The lowest face of the upper chamber (face F3) contacting the upper face of the free decoupler is defined as FSI interface. The other faces of the convex part under the face F1 or F2 contacting with the cage are described as rigid walls. All the faces above the face F1 or F2 touching with the interior faces of the rubber spring are defined as FSI interfaces.

The entrance (face 4) and the exit (face 5) of the inertia track are respectively linked with the exit of the upper chamber (face 1) and the entrance of the lower chamber (face 6) with the command of 'Face Link' of the ADINA. The remaining faces in the inertia track are rigid walls without slip. The face F7 in the upper end of lower chamber contacting the cage is defined as rigid wall without slip. The top face of the low chamber (F8) contacting with the bottom face of the free decoupler is defined as FSI interface. The other faces of the convex part above the face F7 or F6

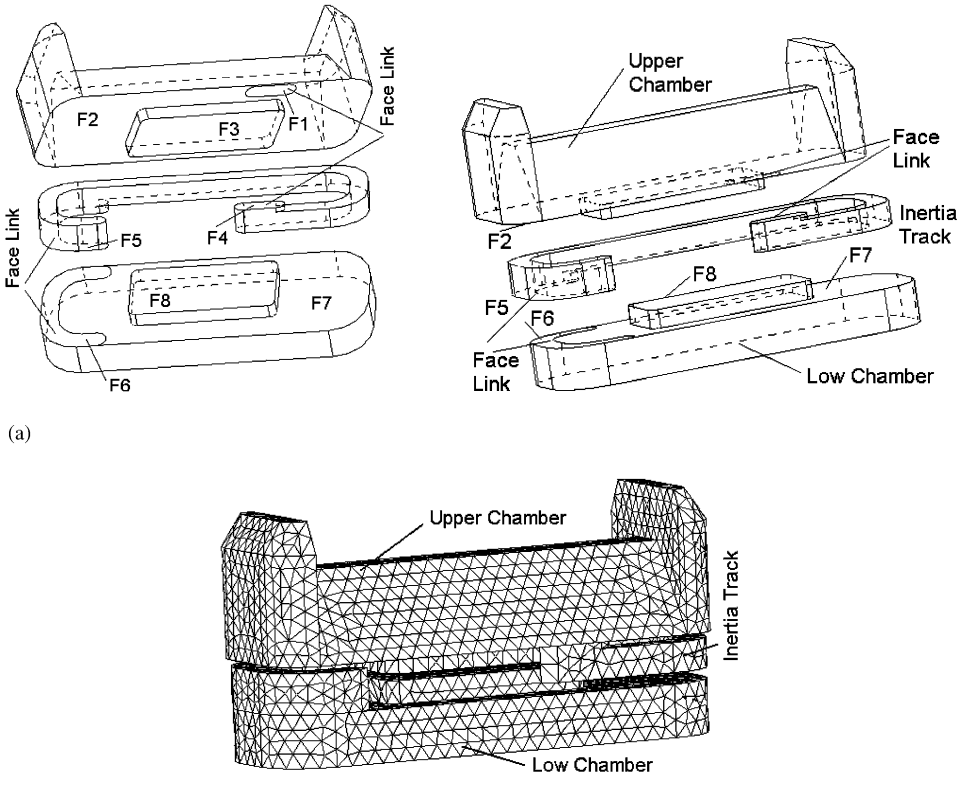

Fig. 22. The fluid model. (a) Geometry model. (b) FEM model.

contacting with the cage are described rigid walls. All the faces below the face F6 or F7 contacting the interior faces of the rubber bellow are defined as FSI interfaces.

The structure model and the fluid model are meshed with 8/1 element (8-node hexahedron element with one pressure variable) and 4/4 element (4-node tetrahedron element with four pressure variables), respectively. The maximum size of the element for the structure and the fluid model are 6 and 5 mm, respectively, and the total numbers of element and node are 27,666 and 13,310, respectively, which includes 18,972 elements and 4615 nodes for the fluid model. The total numbers of degree of freedoms are 53,236.

6. Simulation results of the HEM

6.1. Results of static analysis

The force versus displacement relations in the vertical direction of HEM obtained from FSI model and experiment are shown in Fig. 23. As the figure indicates, the calculation result matches measurement reasonably.

The deformation of the structure and the fluid pressure distribution are given in Fig. 24 when the HEM bears the vertical preload of 2000 N. As Fig. 24 illustrates, the pressure distribution in the chamber and the inertia track is nearly uniform and a pre-pressure exists in the fluid under the preload.

6.2. Results of dynamic analysis

Using the LP model in Section 3 along with the estimated parameters in Section 4 and the fully coupled FSI model in Section 5, the simulated results and experimental data for the mount behavior are compared over the frequency range of 1–200 Hz. The predicted dynamic stiffness and loss angle with the two models and the experimental data for low-frequency and large-amplitude

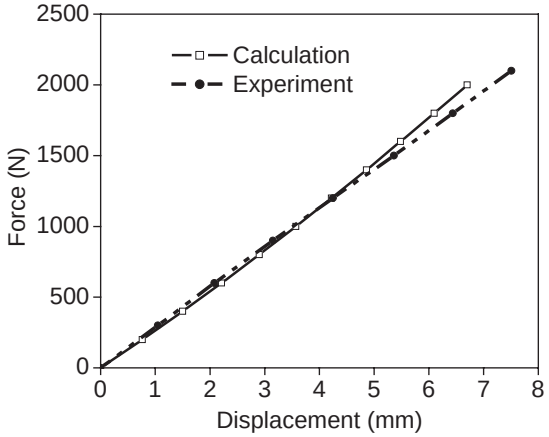

Fig. 23. The force versus displacement of the HEM.

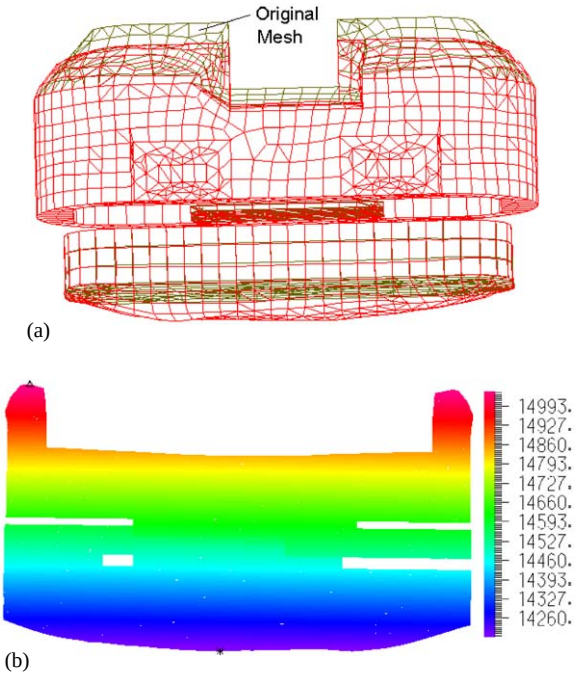

Fig. 24. The deformation of the structure and the fluid pressure. (a) Deformation of the structure. (b) Pressure distribution (Pa).

excitation are shown in Fig. 25. As seen in the figure, the difference of the errors in dynamic stiffness for LP model and FSI model is not obvious, whereas the loss angle estimated from the FSI models is close to the experimental data. The high-frequency response of the HEM from the LP model and experiment are shown in Fig. 26. The agreement of the frequency in peak loss angle and the lowest frequency of the dynamic stiffness surging is significant.

The influence of the parameters on the dynamic stiffness and loss angle can be examined by changing the parameters in the models, and so the performance optimization of the HEM can be realized effectively.

Displacement-time histories of the free decoupler at 10 Hz for 1.0 mm amplitude excitation estimated from the FSI model and the LP model are shown in Fig. 27. It can be seen that the decoupler displacement from the two models is almost the same as that of its physical movement, which demonstrates that the polynomial model for the decoupler is feasible in modelling the dynamic performance of the HEM.

The calculated fluid flow through the inertia track and the decoupler from the LP model at 100 Hz for 0.1 mm amplitude excitation are shown in Fig. 28. As Fig. 28 shows, the fluid volume through decoupler (Q_d) is much larger than the fluid volume through the inertia track (Q_i) for the high-frequency excitation. For such excitations, the HEM often behaves like conventional rubber mounts.

Under the excitation of 10 Hz and 1.0 mm, the estimated pressure distributions of the chambers and the inertia track from the FSI model at different times are shown in Fig. 29.

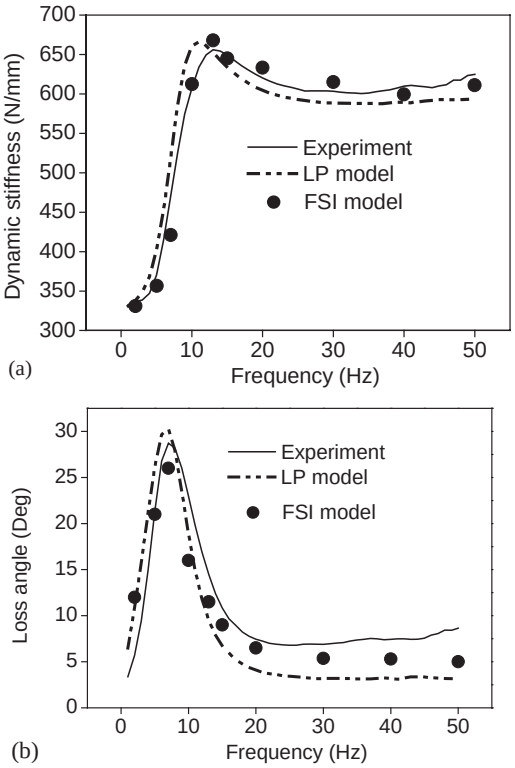

Fig. 25. Low-frequency simulation versus measured response on a mount including a free decoupler and an inertia track (1.0 mm). (a) Dynamic stiffness. (b) Loss angle.

The calculated cross-sectional pressure distribution from the FSI model at different height of the upper chamber for typical excitation frequencies and 1.0 mm excitation amplitude is given in Fig. 30. It can be concluded from Figs. 29 and 30 that the pressure distribution in the upper and lower chamber is nearly uniform, which validates the assumption that the pressure distribution is uniform in the chambers in the LP model. The pressure gradient in the inertia track is notable, which is in coincidence with the mechanism of HEM.

The predicted average velocity of the cross-section of the inertia track and the velocity distributions of horizontal cross-section of the inertia track at different time for 1.0 mm amplitude and 10 Hz frequency excitation from the fully coupled FSI model are given in Figs. 31 and 32, respectively. As Fig. 31 shows, the maximum velocity of the cross-section is 2.54 m/s, whereas the maximum value of the excitation velocity is 62.83×10^{-3} m/s. The fluid velocity of the inertia track is enlarged by roughly 40 times, which is close to the ration of the equivalent piston area of the upper chamber to the cross-sectional area of inertia track, 46.

The simulated upper chamber pressure from the LP model and/or FSI model and the experiment data at 10 Hz for1.0 mm amplitude excitation, and at 100 Hz for 0.2 mm amplitude excitation are indicated in Fig. 33. As Fig. 33(a) indicates, the pressure errors from the FSI model is smaller than that of the LP model, which is predictable since the pre-pressure of the HEM under the preload can be considered in the FSI model. The large errors between the estimated pressure

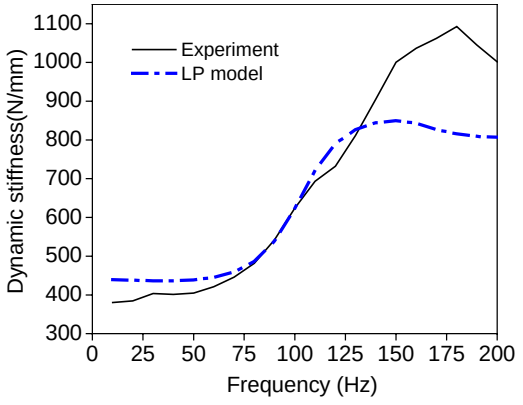

(a) Dynamic stiffness

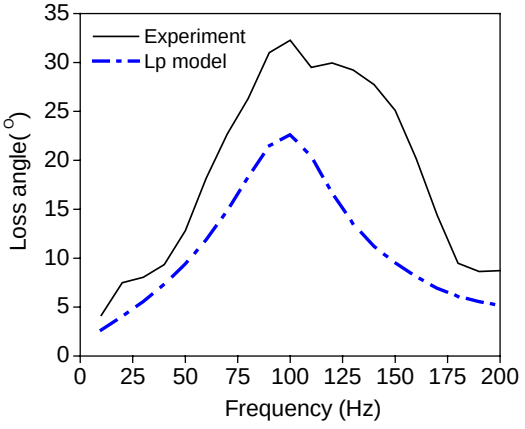

(b) Loss angle

Fig. 26. High-frequency simulation versus measured response on a mount including a free decoupler and an inertia track (0.2 mm).

from LP and experiment attribute to negligence of the pre-pressure of the $P_1(t)$ in the lumped model.

7. Concluding remarks

In this paper, we provide methods for predicting the system parameters in the lumped model of a HEM by using non-linear FEA and FSI FEA and develop a fully coupled FSI model for estimating the response of the HEM. The estimated parameters are compared favorably with the experimental data and/or analytical solutions. The mount responses for both low- and high-frequency excitations are predicted using the LP model along with the calculated system parameters and/or the FSI model. The models predict dynamic stiffness of the HEM in low frequency with less than 15% relative error. The relative error in loss angle with the LP model is less than 20% when the excitation frequency is in the range of 5–20 Hz, whereas the relative error

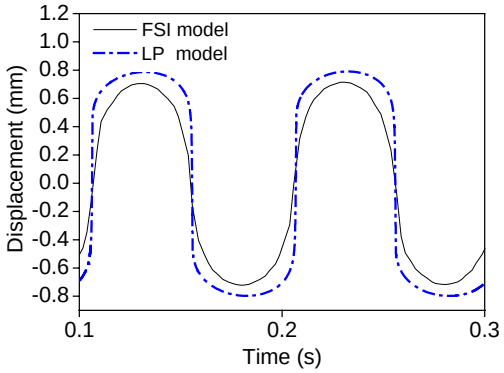

Fig. 27. Time response of the decoupler at 10 Hz for 1.0 mm amplitude.

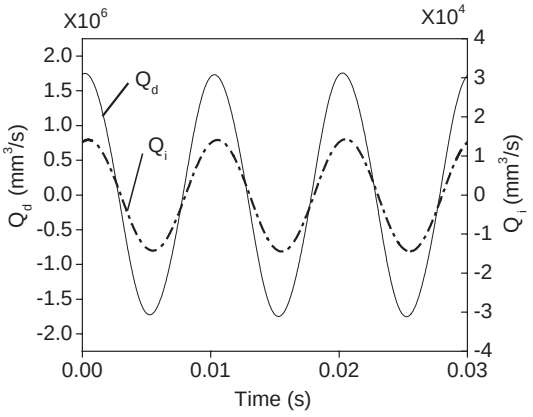

Fig. 28. Time response of flow through the inertia track and the decoupler.

in loss angle with the FSI model is less than 15% when the frequency is in 5–40 Hz. For high-frequency excitation, the peak frequency in loss angle and the lowest frequency for the dynamic stiffness surging can be well predicted with the LP model. Discrepancies between the experiment and results estimated from the LP model are attributed to the following factors: the assumptions made with lumped parameter model assumption, the errors of the system parameters from FEA, the limitation of the upper chamber compliance to static and the negligence of the bulge damping parameter of the upper chamber compliance. Also, gas–liquid phase transformation and cavitation phenomenon [3,4] are not captured in the lumped model.

The LP model and the fully coupled FSI model are used to model the performance; each model has its pros and cons. The advantages of the FSI model over the lumped model are: the static properties of the HEM can be estimated; the pressure distribution in the chambers and the inertia track, and the velocity distribution of the inertia track can be predicted, which validates the assumption of uniform pressure of the chambers in LP model; moreover the shape and size optimization of the HEM can be performed with the FSI model. In the present FSI model, the 3-term Ogden constitutive model is used to characterize the behavior of the rubber spring. The

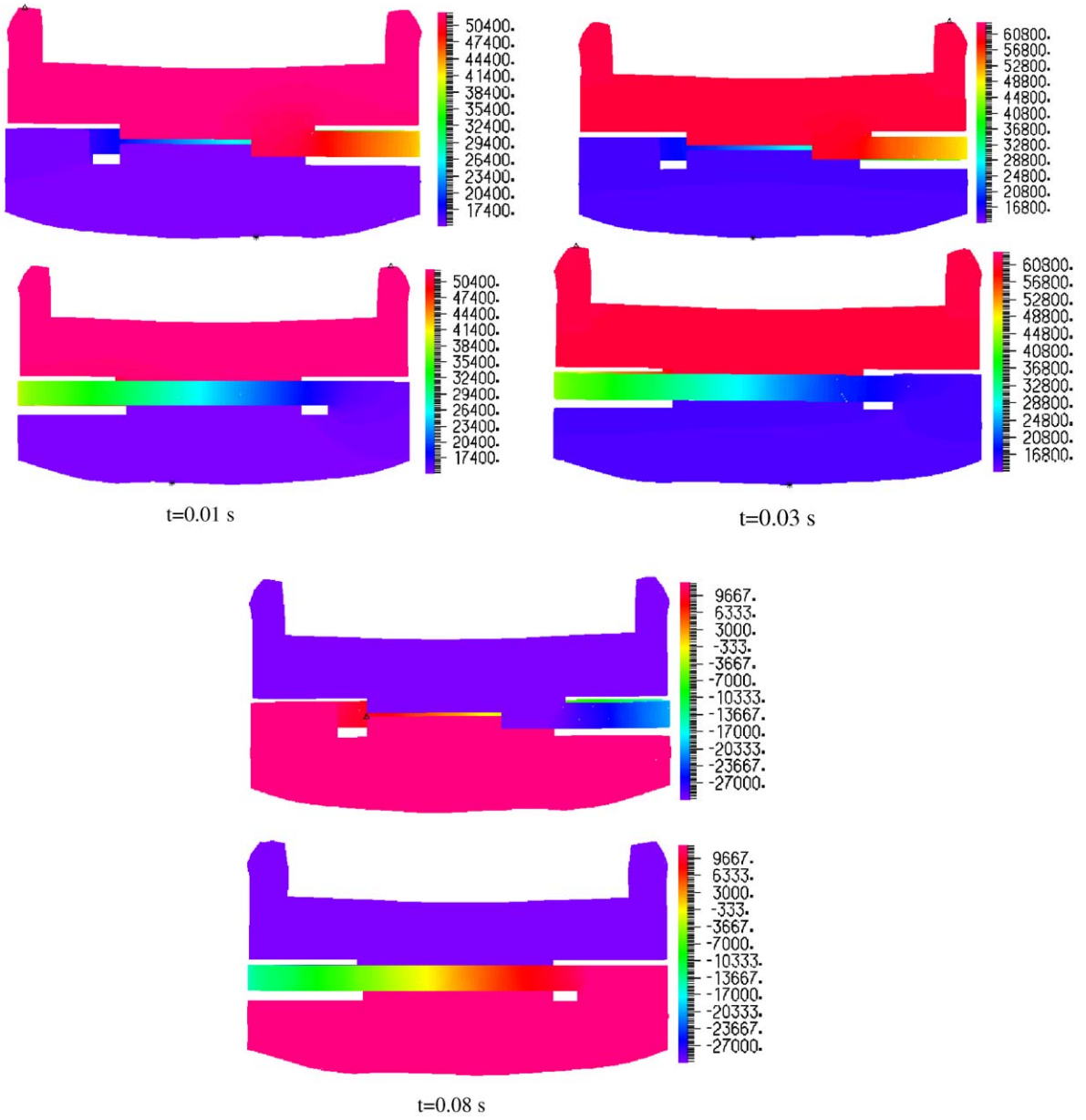

Fig. 29. Pressure distribution (Pa).

constitutive model is only valid for modelling the behaviors of HEM for low-frequency and large-amplitude excitations. New constitutive model for rubber spring, such as visco-hyperelastic or finite linear visco-elasticity model, should be developed in order to simulate the HEM's performances at high-frequency and small-amplitude excitations. Up to now, no such models are available in ADINA program. Fortunately, the use of HEM in automotive powertrain is mainly

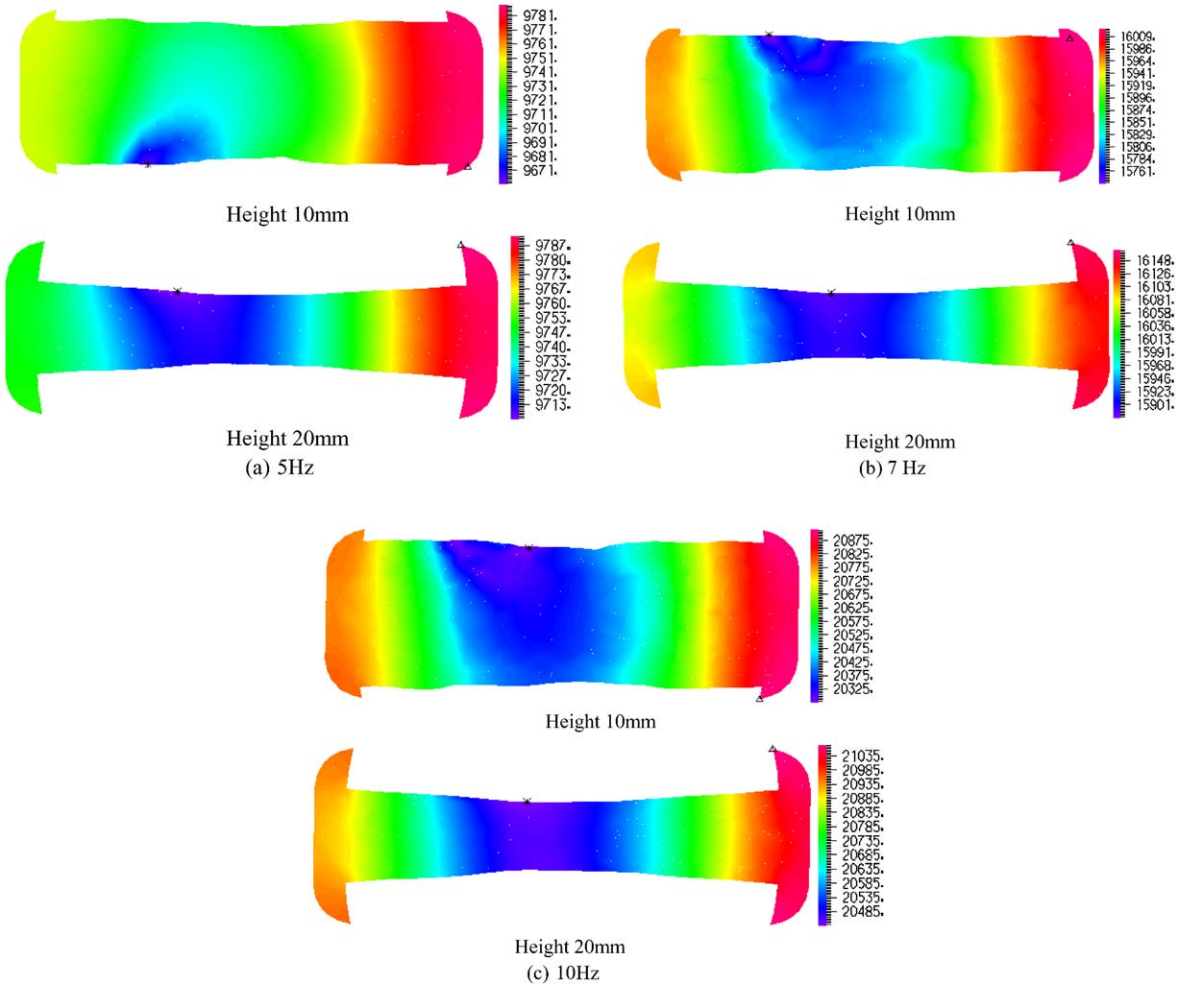

Fig. 30. The pressure distribution at different height of the upper chamber cross-section (Pa).

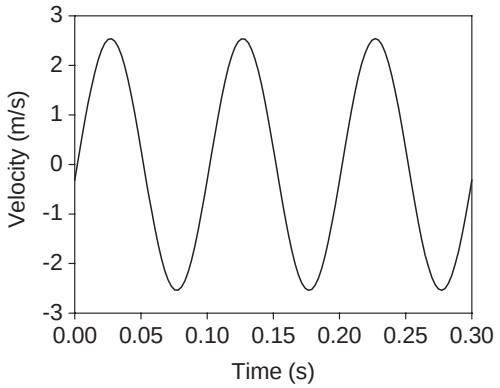

Fig. 31. The average velocity of the cross-section of the inertia track.

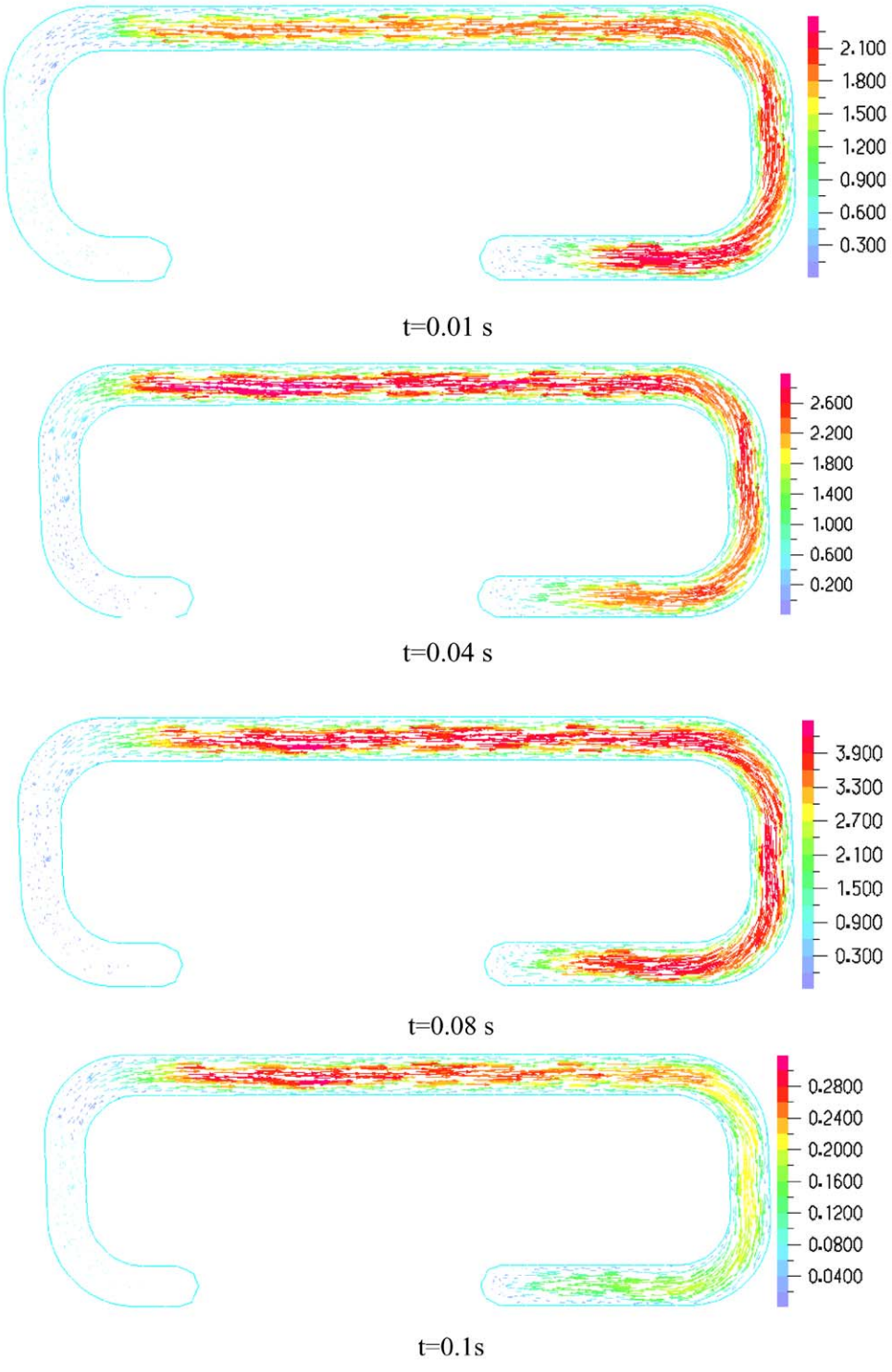

Fig. 32. The velocity distributions of horizontal cross-section of inertia track (m/s) (1 mm, 10 Hz).

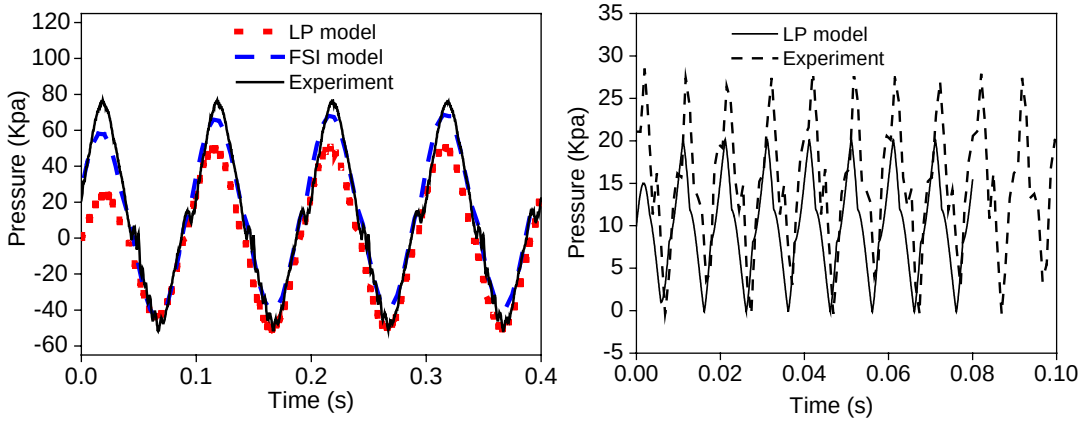

(a) 1.0mm 10Hz (b) 0.2mm 100Hz

Fig. 33. History of the upper chamber pressure.

for isolating vibration from road or engine at idle at the low-frequency range (1–50 Hz) and large amplitude excitation (1–2 mm). So only lower-frequency characteristics are required in the design of the HEM. For high-frequency and small-amplitude excitations, the performance of HEM is inferior to the conventional rubber mount since the HEM's dynamic stiffness and loss angle are larger than that of rubber mount. And in these cases, the function of the HEM should be limited.

The work presented here demonstrates that the methods for estimating the system parameters from FEA and the developed fully coupled FSI model for modelling the HEM are feasible and useful in analyzing and designing of hydraulic mounts. The advantage of the methods proposed in this paper is that no mount prototype or related parts need to be made in the initial design stage, thus the mount design time is greatly reduced. Future work should be carried on the simulation of the high-frequency response of the HEM and performance optimization of the HEM with the FSI model.

Acknowledgements

The project is sponsored by the Research Foundation from the China Ministry of Education, the Tsinghua University, and the Toyota Motor Corporation. The authors are grateful to Dr. A. Khajepour, University of Waterloo for providing us useful references, and Dr. Yanhu Guo, ADINA R&D for his consultations in applying ADINA to the models.

References

[1] Y.H. Yu, N.G. Naganathan, R.V. Dukkipati, A literature review of automotive engine mount systems, *Mechanism and Machine Theory* 36 (2001) 123–142.

[2] Y.H. Yu, S.M. Peelamedu, N.G. Naganathan, R.V. Dukkipati, Automotive vehicle engine mounting systems: a survey, *Journal of Dynamic systems, Measurements, and Control* 123 (2001) 186–194.

[3] A. Geisberger, A. Khajepour, F. Golnaraghi, Nonlinear modeling of hydraulic mounts: theory and experiment, *Journal of Sound and Vibration* 249 (2002) 371–397.
[4] G. Kim, R. Singh, Nonlinear analysis of automotive hydraulic engine mount, *Transactions of the American Society of Mechanical Engineers, Journal of Dynamic systems, Measurements, and Control* 115 (1993) 482–487.
[5] R. Singh, G. Kim, P.V. Ravindra, Linear analysis of automotive hydraulic-mechanical mounts emphasis on decoupler characteristics, *Journal of Sound and Vibration* 158 (1992) 219–243.
[6] G. Kim, R. Singh, A study of passive and adaptive hydraulic engine mount systems with emphasis on non-linear characteristics, *Journal of Sound and Vibration* 179 (1995) 427–453.
[7] J.E. Colgate, C.T. Chang, Y.C. Chiou, W.K. Liu, L.M. Keer, Modeling of a hydraulic engine mount focusing on response to sinusoidal and composite excitations, *Journal of Sound and Vibration* 184 (1995) 503–528.
[8] A.K.W. Ahmed, M.M. Haque, S. Rakhejia, Nonlinear analysis of automotive hydraulic mounts for isolation of vibration and shock, *International Journal of Vehicle Design* 22 (1999) 116–128.
[9] M.F. Golnaraghi, G.N. Jazar, Development and analysis of a simplified nonlinear model of a hydraulic engine mount, *Journal of Vibration and Control* 7 (2001) 495–526.
[10] M. Muller, H.G. Eckel, et al., Reduction of noise and vibration in vehicle by an appropriate engine mount system and active absorbers, SAE technical paper series 960185, 1986.
[11] A.N. Brooks, T.J.R. Hughes, Streamline upwind/Petrov–Galerkin formulations for convection dominated flows with particular emphasis on the incompressible Navier–Stokes equations, *Computer Methods in Applied Mechanics and Engineering* 32 (1982) 199–259.
[12] T.J.R. Hughes, L.P. Franca, G.M. Hulbert, A new finite element formulation for computational fluid dynamics: VIII: the Galerkin/least-square method for advective-diffusive equations, *Computer Methods in Applied Mechanics and Engineering* 73 (1989) 173–189.
[13] J. Donea, A Taylor-Galerkin method for convective transport problems, *International Journal for Numerical Methods in Engineering* 20 (1984) 101–119.
[14] T. Nomura, T.J.R. Hughes, An arbitrary Langangian–Eulerian finite element method for interaction of fluid and a rigid body, *Computer Methods in Applied Mechanics and Engineering* 95 (1992) 115–138.
[15] K.J. Bathe, H. Zhang, M.H. Wang, Finite element analysis of incompressible and compressible fluid flows with free surfaces and structural interaction, *Computers and Structures* 56 (1995) 193–213.
[16] ADINA R&D, Inc. 2001. ADINA Theory and Modeling Guide—ADIN-A and F.
[17] J. Mackerle, Fluid–structure interaction problems, finite element and boundary element approaches—a bibliography (1995–1998), *Finite Elements in Analysis and Design* 31 (1999) 231–240.
[18] D.J. Charlton, Y. Yang, K.K. Teh, A review of methods to characterize rubber elastic behavior for use in finite element analysis, *Rubber Chemistry and Technology* 67 (1994) 481–503.
[19] D.J. Seibert, N. Schoche, Direct comparison of some recent rubber elasticity models, *Rubber Chemistry and Technology* 73 (2000) 366–384.
[20] J.J. Kim, H.Y. Kim, Shape design of an engine mount by a method of parameter optimization, *Computers and Structures* 65 (1997) 725–731.
[21] K.N. Morman Jr., T.Y. Pan, Application of finite-element analysis in the design of automotive elastomeric components, *Rubber Chemistry and Technology* 61 (1988) 503–533.
[22] M.S. Foumani, A. Khajepour, M. Durali, Application of shape memory alloys to a new adaptive hydraulic mount, SAE technical paper series 2002-01-2163, 2002.